COMMUNICATION

Check for updates

Ultramicroporous crosslinked polyxanthene-poly(biphenyl piperidinium)-based anion exchange membranes for water electrolyzers operating under highly alkaline conditions†

Zejun Zheng,[ab] Boxin Xue, (ID) *[a] Jin Yao, (ID)[c] Qingyi He,[c] Zhen Wang[ab] and Jingling Yan (ID) *[ab]

Anion exchange membrane water electrolyzers (AEMWEs) suffer from low efficiencies and durability, due to the unavailability of appropriate anion exchange membranes (AEM). Herein, a rigid ladder-like polyxanthene crosslinker was developed for the preparation of ultramicroporous crosslinked polyxanthene-poly(biphenyl piperidinium)-based AEMs. Due to the synergetic effects of their ultramicroporous structure and microphase-separation morphology, the crosslinked membranes showed high OH$^-$ conductivity (up to 163 mS cm^{-1} at 80 °C). Furthermore, these AEMs also exhibited moderate water uptake, excellent dimensional stability, and remarkable alkaline stability. The single-cell AEMWE based on QPBP-PX-15% and equipped with non-noble catalysts achieved a current density of 3000 mA cm^{-2} at 2.03 V (compared to PiperION's 2.26 V) in 6 M KOH solution at 80 °C, which outperformed many AEMWEs that used platinum-group-metal catalysts. Thus, the crosslinked AEMs developed in this study showed significant potential for application in AEMWEs fed with concentrated alkaline solutions.

New concepts

Green hydrogen holds promise as a carrier of clean energy for sustainable development. The generation of green hydrogen by electrolysis of water is currently the only viable option to store multi gigawatt-levels of electrical energy from intermittent renewable energy sources, such as wind and solar. However, both acidic and alkaline electrolyzers have several drawbacks, which hamper their large-scale implementation. An anion exchange membrane water electrolyzer (AEMWE), which is new, cost-efficient, and energy-efficient, can be used for the production of high-purity hydrogen. Nonetheless, the lack of reliable anion exchange membranes (AEMs) hampers the broader application scope of AEMWE. In this work, ultramicroporous crosslinked polyxanthene-poly(biphenyl piperidinium)-based AEMs with high ionic conductivity, low water uptake, favorable mechanical robustness, and exceptional alkaline stability have been reported. This could probably address the limitations associated with current AEMs. Furthermore, the resultant AEMWE single cells showed high performance and good durability under highly alkaline conditions, demonstrating their potential for scalable and economical production of green hydrogen.

1. Introduction

Low-temperature water electrolysis using a membrane is one of the most promising technologies to realize efficient utilization of intermittent renewable energies, such as wind and solar.[1,2] Alkaline water electrolyzers (AWEs), based on traditionally porous diaphragm membranes, suffer from low rates of hydrogen production and high sensitivity to differential pressures.[3] In contrast, electrolyzers based on ion exchange membranes permit the design of a zero-gap system with resistant structural properties at high differential pressures (200–400 psi).[4] Furthermore, highly conductive ion exchange membranes enable the operation of electrolyzers at high constant current densities and thereby achieve high rates of hydrogen production.[5]

Currently, proton-exchange membrane water electrolyzers (PEMWEs) are the incumbent technology in this category.[6,7] However, the high cost of platinum-group-metal (PGM) catalysts, acid-tolerant stack hardware, and perfluorosulfonic acid membranes significantly compromise the competitiveness of PEMWEs.[8] More recently, anion exchange membrane water electrolyzers (AEMWEs), which combine the merits of AWEs and PEMWEs, have attracted considerable attention.[9] For example, alkaline operating conditions in AEMWEs enable the use of inexpensive non-noble catalysts (Ni, Mo, Fe, *etc.*), whose performance is comparable or even better than that of PGM-based catalysts.[10,11] The low ohmic loss owing to the highly conductive and thin AEMs further improves the electrolytic performance of AEMWEs. However, the application scope of AEMWEs is still restricted due to the unsatisfactory

[a] *Ningbo Institute of Materials Technology and Engineering, Chinese Academy of Sciences, Ningbo 315201, China. E-mail: xueboxin@nimte.ac.cn, jyan@nimte.ac.cn*

[b] *University of Chinese Academy of Sciences, Beijing 100049, China*

[c] *Ningbo Sino-Tech Hydrogen Membrane Technology Co., Ltd, Ningbo 315207, China*

† Electronic supplementary information (ESI) available. See DOI: https://doi.org/10.1039/d4mh00836g

properties of AEMs, such as low conductivity, insufficient physical and chemical stability, and poor durability.[1,12]

The ionic conductivity of AEMs determines the performance of AEMWEs, wherein higher conductivity results in higher current density output at a given voltage. The inherent slower migration rate of OH^- inevitably is responsible for the lower conductivity of AEMs than PEMs.[13,14] Increasing the ion exchange capacity (IEC) is a straightforward approach to achieve high OH^- conductivity. However, excessively high IECs significantly increase water uptake and cause membrane swelling,[15] which compromises the mechanical properties and long-term durability of AEMs. Engineering of morphology can address the trade-off between ionic conductivity and mechanical robustness. For example, rational design of polymer architecture (e.g., block copolymers, side-chain grafting, and crosslinking) can induce the formation of well-developed microphase-separated structures and ion transport channels, which can achieve high conductivity at relatively low IEC values.[16–19] However, the aforementioned strategies usually involve complex synthetic processes. Furthermore, irregular and isolated ion-conductive regions and extensive hydrophobic polymer matrices can still retard the rapid transportation of ions.[20]

Recently, various intrinsically microporous AEMs were developed to improve the OH^- conductivity. Rigid and twisted units, such as m-terphenyl,[20,21] Tröger's base,[22] xanthene,[23] spirobisindane,[24,25] and triptycene,[26] were incorporated into AEMs, which produced inefficient chain packing that led to the generation of ion channels. For example, Xu et al. prepared a series of poly(piperidinium)-based AEMs containing well-connected and uniformly distributed ultramicropores, by adjusting the ratios of m-terphenyl and p-terphenyl.[20] The microporous structures served as channels for ion transport, and the AEMs exhibited high OH^- conductivity of 217.0 mS cm^{-1} with a low swelling ratio of <15% at

90 °C. The assembled AEMs showed excellent performance and durability in AEMWEs. Lee et al. reported triptycene-branched poly(aryl-co-aryl piperidinium)s, which showed high hydroxide conductivity (193.5 mS cm^{-1} at 80 °C), excellent alkaline stability, and good mechanical and dimensional stability, due to the branched network structures and high fractional free volume (FFV).[26] Furthermore, by using precious and non-noble metal catalysts, the AEMWEs based on these AEMs achieved unprecedented current densities.

The use of rigid and twisted macromolecular crosslinkers has also been considered an alternative strategy to access microporous AEMs. Kim et al. reported crosslinked AEMs, based on an intrinsically microporous spirobisindane crosslinker and SEBS polymer.[27] The obtained AEMs had low swelling, high tensile strength, and excellent alkaline stability. The results of single-cell AEMWE testing indicated that these membranes outperformed the commercial FAA-3-50 membrane by 176% by achieving a current density of 1.905 A cm^{-2} at 2.0 V (1.083 A cm^{-2} for FAA-3-50). Poly(aryl piperidine)s and their copolymers have been extensively used for AEM preparation. They are readily prepared via a single-step Friedel–Crafts polymerization of aromatics and N-methyl-4-piperidone.[17,19,20,24,26] Crosslinked microporous membranes can be constructed using poly(aryl piperidine)s and macromolecular crosslinkers. However, there are few reports on this topic and the structures of intrinsically microporous macromolecular crosslinkers require optimization.

Polyxanthenes (PXs) are a new class of polymer skeletons for ion exchange membranes.[28–30] Their deficient chain packing, due to the rigid and contorted xanthene moieties, is useful for the construction of ion transport channels and enhancement of ion conductivity.[28,30] Herein, a novel intrinsically microporous PX crosslinker with a rigid ladder-like backbone structure and
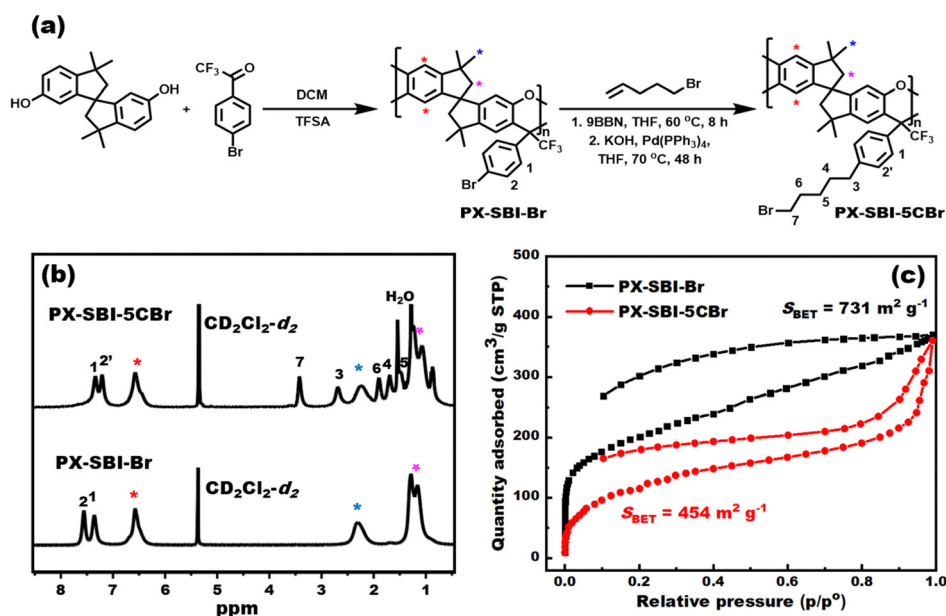

Fig. 1 (a) Synthetic route, (b) ^{1}H NMR spectra, and (c) N_2 adsorption/desorption isotherms of PX-SBI-Br and PX-SBI-5CBr.

pendent bromopentyl groups, has been reported. Next, a series of crosslinked AEMs, based on the PX crosslinker and poly(biphenyl piperidine) (PBP), were subsequently developed. The crosslinking network prevented the dense packing of polymer chains that induced the formation of ultramicroporous structures. It also increased ionic conductivity, mechanical robustness, and chemical stability of the AEMs. The influence of polyxanthene content (5, 10, and 15%) on the AEM properties was systematically investigated in terms of water absorption, dimensional stability, morphology, ion conductivity, and alkaline stability. The structure–property relationship and AEMWE performance of these AEMs were also elucidated.

2. Results and discussion

2.1 Synthesis and characterization of the polyxanthene macromolecular crosslinker

In this study, the macromolecular crosslinker, PX-SBI-5CBr, was prepared in two steps. First, the brominated PX precursor (PX-SBI-Br) was synthesized *via* the polyhydroxyalkylation–cyclodehydration reaction between 3,3,3′,3′-tetramethyl-1,1′-spirobiindane-6,6′-dihydroxy (SBI) and 4′-bromo-2,2,2-trifluoroacetophenone (Fig. 1a). The polymerization proceeded smoothly, affording the polymer with a weight-average molecular weight (M_w) of 122 kDa and polydispersity index (PDI) of 2.18. Next, the bromopentyl groups were incorporated *via* Suzuki coupling reaction of PX-SBI-Br with *B-n*-pentyl-9-borabicyclo[3.3.1]-nonane, which was generated *in situ* through the hydroboration of 5-bromo-1-pentene with 9-borabicyclo[3.3.1]nonane (9BBN).

The structures of PX-SBI-Br and PX-SBI-5CBr were confirmed by ^1H NMR analysis. In the ^1H NMR spectrum of PX-SBI-Br, aromatic protons of the PX backbone appeared at 6.56 ppm, whereas signals for bromo-phenyl segments appeared at 7.56 and 7.36 ppm. Meanwhile, the signals at 2.29 and 1.14–1.26 ppm were assigned to the aliphatic protons in SBI units. After the grafting reaction, five new signals appeared at 3.44, 2.73, 1.92, 1.72, and 1.53 ppm, which were assigned to the alkyl bromide side chains in PX-SBI-5CBr. The integral ratio of these five peaks was approximately 1 : 1 : 1 : 1 : 1 as expected. Furthermore, peak 2 in the spectrum of PX-SBI-Br at 7.56 ppm shifted to 7.24 ppm in that of PX-SBI-5CBr. These results confirmed the successful grafting of alkyl bromide side chains.

The intrinsic microporosities of PX-SBI-Br and PX-SBI-5CBr were validated by their N_2 adsorption/desorption isotherms (Fig. 1c). A high N_2 uptake at low pressure indicated the existence of large number of micropores. Moreover, the Brunauer–Emmett–Teller (BET) surface areas (S_{BET}) of PX-SBI-Br and PX-SBI-5CBr were 731 and 454 m^2 g^{-1}, respectively. The lower S_{BET} value of PX-SBI-5CBr as compared to PX-SBI-Br could be explained on the basis of the pore-filling effect of bromopentyl side chains.

2.2 Preparation of crosslinked polyxanthene-poly(biphenyl piperidinium)-based AEMs

Jannasch *et al.* were the first to report the preparation of iodomethane-quaternized PBP. Meanwhile, its extremely high IEC (3.55 mmol g^{-1}) caused excessive membrane swelling and led to poor mechanical properties.[31] Crosslinking has been found to be an effective strategy to address these issues.[32,33] In this work, a series of crosslinked AEMs (QPBP-PX-*x*) were prepared by chemically crosslinking PBP with PX-SBI-5CBr. The crosslinking occurred between the –CH$_2$Br group in PX-SBI-5CBr and the piperidine group in PBP. The extent of crosslinking was adjusted by varying the ratios of –CH$_2$Br and piperidine. The remaining piperidine functionalities were further quaternized by iodomethane (Scheme 1). Finally, the AEMs were obtained after drying the colloidal solutions on glass substrates (Fig. S3, ESI†).

The crosslinked AEMs were characterized by using FT-IR spectroscopy (Fig. S4a, ESI†). The absorption band at 560 cm^{-1}, assigned to the C–Br stretching vibrations of –CH$_2$Br, disappeared completely in the spectrum of QPBP-PX-*x*, which confirmed the crosslinking reaction. Meanwhile, the intensities of the peaks at ∼1150 cm^{-1}, corresponding to the C–O–C stretching, increased gradually with increase in PX-SBI-5CBr content. Furthermore, the characteristic peaks for –OH stretching and C–N stretching vibrations in quaternary ammonium hydroxide were observed at 3430 and 1383 cm^{-1}, respectively.[34] After crosslinking, the AEMs were insoluble in *N*-methylpyrrolidone (NMP) even after heating at 80 °C for 8 hours (Fig. S4b, ESI†). In addition, the gel fractions of QPBP-PX-5%, QPBP-PX-10%, and QPBP-PX-15% were in the range of 79.6–83.0% (Table 1). The aforementioned results confirmed the crosslinking reactions between PX-SBI-5CBr and PBP.
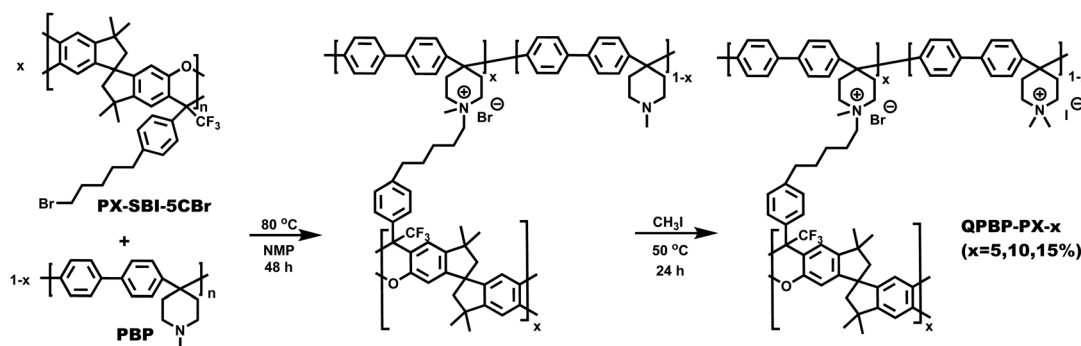
Scheme 1 Route to the syntheses of QPBP-PX-*x* AEMs.

Table 1 Properties of QPBP-PX-5%, QPBP-PX-10%, and QPBP-PX-15%

| AEM | IEC (mmol g^{-1}) | | Gel fraction^c (%) | ρ (g cm^{-3}) | FFV | Water uptake (%) | | Swelling ratio (%) | | OH$^-$ Conductivity (mS cm^{-1}) | |
	Theor.^{a}	Titrated^b				30 °C	80 °C	30 °C	80 °C	30 °C	80 °C
QPBP-PX-5%	3.23	3.18	79.6	1.252	0.075	61.5	88.0	15.3	18.5	77.0	129.0
QPBP-PX-10%	3.02	2.94	82.2	1.196	0.119	23.7	71.2	14.5	15.7	56.7	155.6
QPBP-PX-15%	2.81	2.69	83.0	1.137	0.165	18.1	40.3	8.8	9.7	89.2	163.0

^{a} Theoretical value assuming 100% conversion. ^{b} Measured by titration. ^{c} Percentage of residual mass after treatment in NMP at 80 °C for 12 h.

2.3 IEC and microstructures

The theoretical IEC values of QPBP-PX-5%, QPBP-PX-10%, and QPBP-PX-15% were 3.23, 3.02, and 2.81 mmol g^{-1}, respectively, assuming stoichiometric crosslinking and complete quaternization. These values were consistent with the measured IECs (Table 1). The FFVs of QPBP-PX-5%, QPBP-PX-10%, and QPBP-PX-15%, calculated from their bulk densities, were 0.075, 0.119, and 0.165, respectively. The FFV increased with increase in PX-SBI-5CBr content, due to the combined effects of higher FFV of PX-SBI-5CBr than PBP, as well as the increase in crosslinking density.

The surface areas and pore size distributions of the crosslinked AEMs were determined from their CO_2 adsorption isotherms (Fig. 2a and b). The surface areas of QPBP-PX-5%, QPBP-PX-10%, and QPBP-PX-15 were 37.5, 98.4, and 92.8 m^2 g^{-1}, respectively. The apparently higher surface areas of QPBP-PX-10% and QPBP-PX-15% than QPBP-PX-5% was attributed to the increase in crosslinking densities and PX-SBI-5CBr contents. QPBP-PX-5% showed a bimodal pore width distribution of <1 nm ultramicropores, centered at 0.56 and 0.78 nm. In contrast, QPBP-PX-10% and QPBP-PX-15% showed trimodal pore width distributions, which could be due to the increase in crosslinking densities. Despite their similar surface areas, QPBP-PX-15% had smaller pore size than QPBP-PX-10%, which could be ascribed to the difference in their internal crosslinking structures. The H_2 and O_2 permeabilities of these AEMs followed the order of QPBP-PX-15% > QPBP-PX-10% > QPBP-PX-5% (Fig. 2c and Table S1, ESI†), which was consistent with the trend of their FFV. Moreover, the crosslinked AEMs exhibited apparently lower gas permeabilities, as compared to the commercial PiperION AEM and other reported AEMs.[35] Specifically, the H_2 and O_2 permeabilities of QPBP-PX-15% was only around 2/3 and 1/2, as of those of PiperION, respectively. These results indicated that the presence of sub-nanometer pores (<1 nm) in these crosslinked AEMs did not give rise to significant gas permeation issues.

The microstructures of crosslinked AEMs were further studied by small angle X-ray scattering (SAXS), atomic force microscopy (AFM), and transmission electron microscopy (TEM). The maximum scattering vector (q_{max}) values of QPBP-PX-5%, QPBP-PX-10%, and QPBP-PX-15% in the SAXS profiles (Fig. 3a–c) were 2.77, 2.42, and 2.38 nm^{-1}, which corresponded to the characteristic domain sizes (d-spacing) of 2.30, 2.60, and 2.64 nm, respectively. The d-spacing values increased gradually as the crosslinking degree increased. This could be explained by the fact that high crosslinking degree promoted the aggregation of ion clusters and increased the cluster sizes. Moreover, intensities of the ionomer peaks of QPBP-PX-10% and QPBP-PX-15% were obviously higher than that of QPBP-PX-5%. This could be attributed to the better inter-connectivity between their ionic channels.[36] Fig. 3d–f show the AFM images of QPBP-PX-5%, QPBP-PX-10%, and QPBP-PX-15%. Distinctive microphase-separated structures were observed for these AEMs, wherein dark regions represented the hydrophilic domains (ion clusters) and the bright regions represented the hydrophobic domains (polymer backbones).[34] The distribution of ion cluster in QPBP-PX-5% was isolated and uniform. In contrast, the ion clusters in QPBP-PX-10% and QPBP-PX-15% were larger and more connected. These distinctions were also seen in the TEM images (Fig. 3g–i). It could be explained by the fact that an increase in crosslinking degree narrowed the gaps between polymer chains and thus promoted the aggregation of ionic groups. The well-defined microphase-separated morphologies and good connectivity of ion channels were expected to enhance the conductivity of the AEMs.
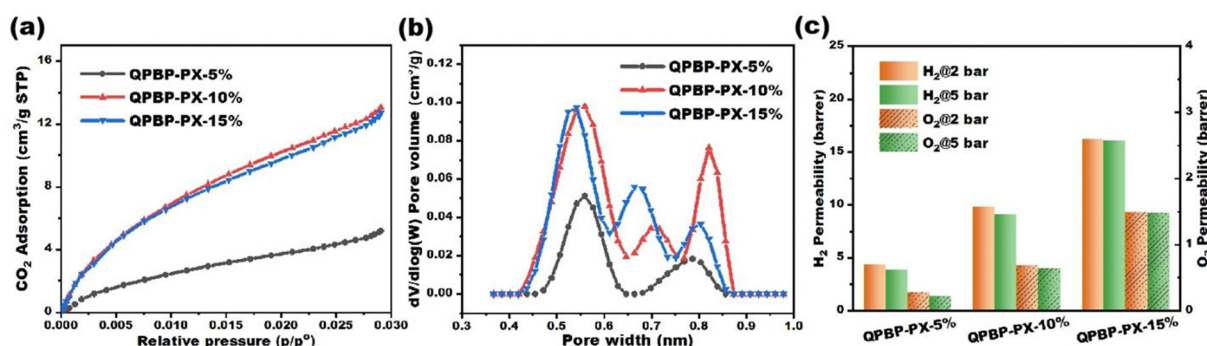

Fig. 2 (a) CO_2 adsorption isotherms, (b) pore size distributions, and (c) H_2 and O_2 permeabilities of QPBP-PX-5%, QPBP-PX-10%, and QPBP-PX-15%.
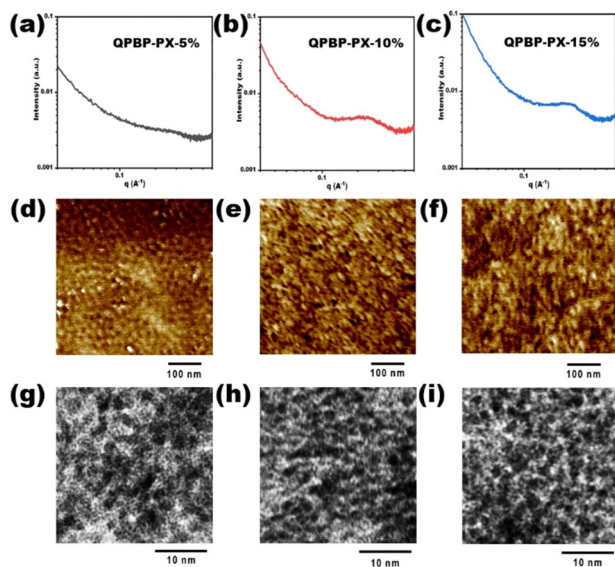
Fig. 3 (a)–(c) SAXS profiles, (d)–(f) AFM phase images, and (g)–(i) TEM images of QPBP-PX-5%, QPBP-PX-10%, and QPBP-PX-15%.

Fig. 4 (a) WU and (b) SR of QPBP-PX-x at 30, 60, and 80 °C. (c) Temperature dependence of OH⁻ and Cl⁻ conductivities of QPBP-PX-5%, QPBP-PX-10%, and QPBP-PX-15%. (d) Comparison of QPBP-PX-15% with commercial PiperION and earlier reported poly(aryl piperidinium) AEMs.[20,27,33,35,38–41]

2.4 Thermal and mechanical properties

For applications in AEMWE, AEMs should possess excellent thermal and mechanical properties. Stress–strain curves were plotted to evaluate the mechanical properties of QPBP-PX-x (Fig. S5a, ESI†). The crosslinked AEMs had tensile strengths and elongation-at-break values in the range of 30–42 MPa and 18–39%, respectively (Fig. S5a, ESI†). The crosslinked AEMs had tensile strength, modulus, and elongation-at-break values in the range of 30–42 MPa, 0.158–0.304 GPa, and 18–39%, respectively (Table S2, ESI†). Apparently, the mechanical properties increased with increase in the degree of crosslinking, which was consistent with the results of crosslinked AEMs reported in the literature.[27] The thermogravimetric (TG) curves of crosslinked AEMs in the OH⁻ form (Fig. S5b, ESI†) showed multiple-step weight loss patterns. The initial weight loss below 200 °C was attributed to the removal of absorbed water. The second stage of weight loss occurred in the temperature range of 200–300 °C, which corresponded to the degradation of piperidinium groups. Finally, the weight loss above 300 °C was ascribed to the decomposition of polymeric backbones. The glass transition temperatures (T_g) of these AEMs, as determined by dynamic mechanical analysis (DMA), followed the trend of QPBP-PX-15% (366 °C) > QPBP-PX-10% (329 °C) > QPBP-PX-5% (306 °C) (Fig. S5c, ESI†). QPBP-PX-15% showed the highest T_g, since it had the highest PX content and crosslinking density. In brief, the mechanical performance and thermal stability of the crosslinked AEMs could meet the requirements for AEMWE applications.

2.5 Water uptake, swelling ratio, and conductivity

For ion-exchange membranes, appropriate water uptake (WU) helps to improve the connectivity of ion transport channels and facilitates rapid ion conduction through the Grotthus mechanism. However, excessive WU and swelling can dilute the ionic
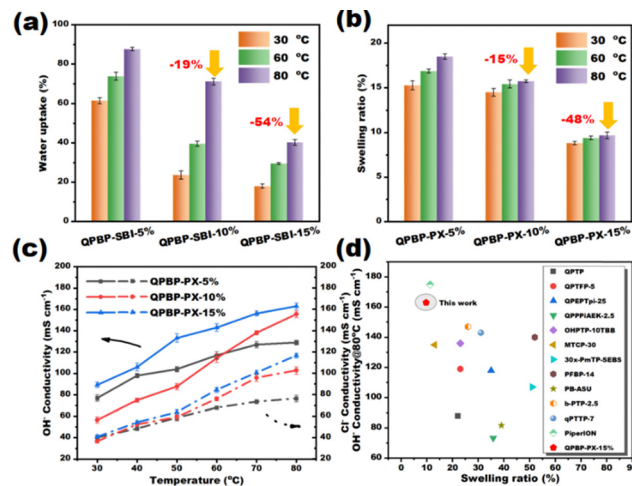
groups and deteriorate the ion conductivity and mechanical properties of the membrane.[37] The WU and swelling ratios (SR) of the QPBP-PX-x AEMs were evaluated at 30, 60, and 80 °C (Fig. 4a and b). The WU and SR values of QPBP-PX-5% were maximum, owing to its highest IEC and lowest crosslinking degree. As expected, the WU and SR values decreased as the degree of crosslinking increased. For example, compared with QPBP-PX-5%, the WU of QPBP-PX-10% and QPBP-PX-15% at 80 °C were 19% and 54% lower than that of QPBP-PX-5%, respectively. Meanwhile, their SR were 15% and 48% lower than that of QPBP-PX-5%, respectively. This was attributed to the reduced IEC values and increased crosslinking degrees of QPBP-PX-10% and QPBP-PX-15%. Despite their high IECs, the crosslinked AEMs exhibited moderate water absorptivities and excellent dimensional stability, due to the presence of cross-linked structures.

The OH⁻ and Cl⁻ conductivities of QPBP-PX-x AEMs were measured at 30, 40, 50, 60, 70, and 80 °C (Fig. 4c). Ion conductivity is dependent on several factors, such as IEC, WU, microscopic phase separation, etc. In general, a membrane with higher IEC exhibits higher ionic conductivity. However, in this study, QPBP-PX-15% exhibited the highest conductivity despite its lowest IEC. Specifically, its Cl⁻ and OH⁻ conductivities were 163.0 and 120.0 mS cm⁻¹ at 80 °C, respectively. This could be due to its lowest WU that could increase the ion concentration and its most pronounced microphase-separated morphology that could promote the formation of ion transport channels. In contrast, in spite of having highest IEC (3.20 mmol g⁻¹), QPBP-PX-5% showed the lowest OH⁻ conductivity below 60 °C. This can be explained by the "dilution effect" as a result of its excessive WU, which could outbalance the positive effect of high IEC. Furthermore, the SR of QPBP-PX-15% with respect to its OH⁻ conductivity was compared with commercial PiperION and other reported poly(aryl piperidinium) AEMs reported in the literature (Fig. 4d).[20,27,33,35,38–41] QPBP-PX-15% showed
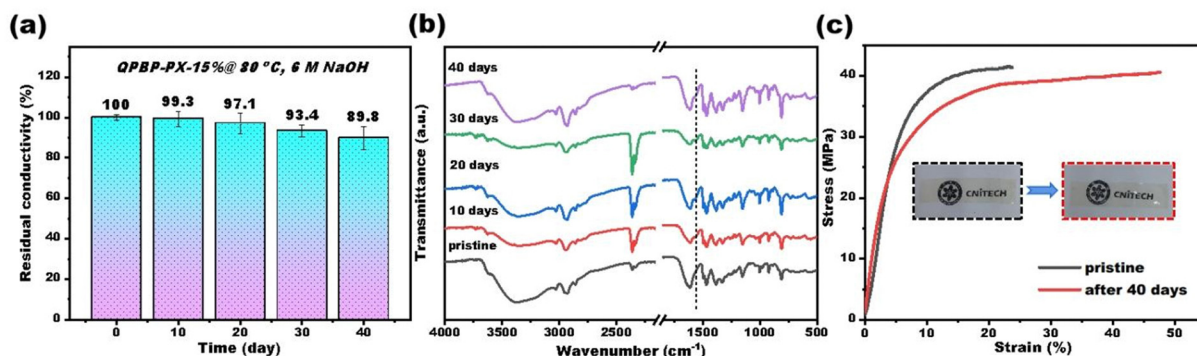
Fig. 5 (a) Residual conductivity, (b) FTIR spectra, and (c) mechanical properties of QPBP-PX-15% after aging in 6 M NaOH at 80 °C.

significantly high conductivity at low swelling ratio, implying the positive effects of the rigid PX crosslinker.

2.6 Alkaline stability

Alkaline stability of AEMs is essential for the long-lifespan of electrochemical devices. Majority of AEMs still suffer from severe deformation and even fracture after alkali aging, especially in harsh conditions, such as high temperatures and high-pH environments.[42] Accelerated testing of *ex situ* chemical stability was performed by immersing QPBP-PX-15% in 6 M NaOH at 80 °C for 40 days. The ion conductivity was measured before and after the testing. The QPBP-PX-15% membrane retained 89.8% of its original conductivity after 40 days of treatment (Fig. 5a). The decrease in ion conductivity could be attributed to the ring-

opening E2 elimination reactions, which could be validated by the appearance of a new peak at ~ 1566 cm^{-1} in the FT-IR spectra (vibrations of carbon–carbon double bond) (Fig. 5b). Furthermore, the QPBP-PX-15% membrane remained transparent and retained 97.8% of its original mechanical strength after testing (Fig. 5c), which further demonstrated its excellent chemical stability. This could be ascribed to the rigid and crosslinked structures of QPBP-PX-15%, which reduced water absorption, thereby preventing the nucleophilic attack of OH$^-$ ions.

2.7 Water electrolysis performance

A PGM-free water electrolyzer was assembled by sandwiching QPBP-PX-15% directly between two commercial Ni-based electrodes (anode: Ni foam, cathode: Ni–Mo–Al). The effects of
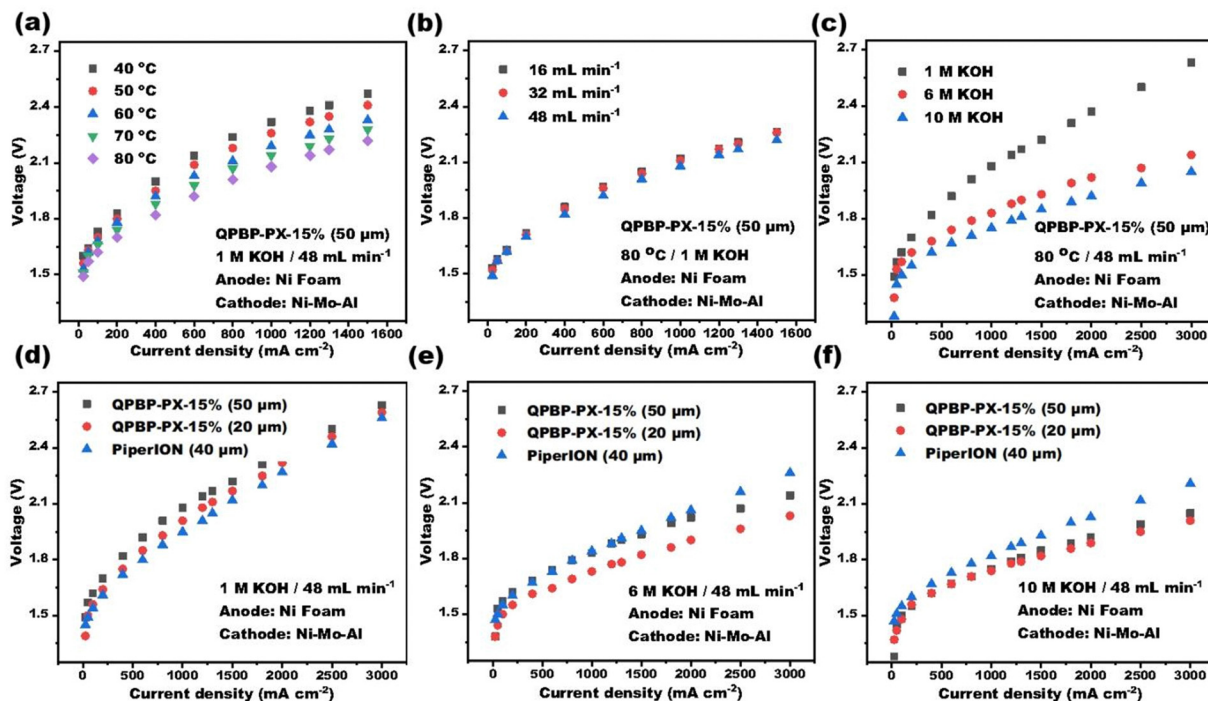

Fig. 6 I–V polarization curves of QPBP-PX-15% based AEMWE with varying (a) temperatures, (b) flow rates of circulating alkaline solution, and (c) concentrations of KOH solution; I–V polarization curves of AEMWEs based on QPBP-PX-15% (50 μm), QPBP-PX-15% (20 μm), and PiperION (50 μm) in (d) 1 M, (e) 6 M, and (f) 10 M KOH solutions at a cell temperature of 80 °C and flow rate of 48 mL min^{-1}.

Table 2 Comparison of the electrolysis performance of QPBP-PX-15%-based AEMWE with those based on reported AEMs

AEM	Catalysts		Ionomer		Test conditions	Performance	Ref.
	Anode	Cathode	Anode	Cathode			
QPBP-PX-15%	Ni foam	Ni–Mo–Al	None	None	80 °C, 6 M KOH	3000 mA cm^{-2}@2.03 V	This work
PiperION	Ni foam	Ni–Mo–Al	None	None	80 °C, 6 M KOH	3000 mA cm^{-2}@2.26 V	This work
PPTQ	NiFe foam	NiMo foam	None	None	80 °C, 5 M KOH	1940 mA cm^{-2}@2.0 V	43
30×-PIM-SEBS	IrO$_2$	Pt/C	FAA-3-SOLUT-10	FAA-3-SOLUT-10	70 °C, 1 M KOH	1905 mA cm^{-2}@2.0 V	27
FAA-3-50	IrO$_2$	Pt/C	FAA-3-SOLUT-10	FAA-3-SOLUT-10	70 °C, 1 M KOH	1083 mA cm^{-2}@2.0 V	27
PFTP-13	Ni–Fe	Ni–Fe	None	None	80 °C, 1 M KOH	1760 mA cm^{-2}@2.0 V	46
MTCP-50	NiFe	Pt/Ru/C	MTCP-50-0%	MTCP-50	90 °C, 1 M KOH	5400 mA cm^{-2}@1.8 V	20
HTMA-DAPP	IrO$_2$	Pt–Ru	TMA-70	TMA-70	85 °C, pure water	2000 mA cm^{-2}@1.9 V	5
PBP	Ni-foam	Pt/C	None	PiperION	60 °C, 1 M KOH	1250 mA cm^{-2}@2.0 V	45
PAP-TP-85	Ni$_{0.5}$Co$_{0.5}$Fe$_2$O$_4$	Pt/C	TP-85	TP-85	60 °C, pure water	500 mA cm^{-2}@2.0 V	47
C-QPAP-2-QPPO	IrO$_2$	Pt/C	None	None	80 °C, 1 M KOH	1440 mA cm^{-2}@2.0 V	34
PAP-TP-85	IrO$_2$	Pt/C	None	QP$_2$-CF$_3$-3	80 °C, 1 M KOH	2500 mA cm^{-2}@1.95 V	25
PBI-bisPip-2.5	Ni foam	Ni foam	None	None	80 °C, 2 M KOH	358 mA cm^{-2}@2.0 V	48

operating temperature, flow rates of circulating alkaline solution, and alkaline solution concentrations on the electrolysis performance were systematically investigated and the polarization curves were plotted, as shown in Fig. 6. As expected, the electrolysis performance gradually improved as the temperature was increased (Fig. 6a). Specifically, the current density increased by ∼100%, as the temperature was ramped from 40 to 80 °C (0.53 A cm^{-2} to 1.1 A cm^{-2} at 2.1 V). This could be attributed to the acceleration in ion transfer and kinetics at high temperatures.[43] The electrolysis performance also improved with increase in the flow rate of circulating alkaline solution (Fig. 6b). A high flow rate could promote timely discharge of the generated gas bubbles, minimize mass transport losses, and thus increase cell efficiency.[44] For a fixed current density, increase in KOH concentration could significantly decrease the input voltage (Fig. 6c). For instance, at a current density of 3000 mA cm^{-2}, the voltage exhibited a decrease from 2.63 V to 2.14 and 2.05 V with an increase in KOH concentration from 1 M to 6 M and 10 M, respectively, indicating that higher KOH concentrations can enhance electrolysis efficiency.

Furthermore, the single-cell AEMWE performances of QPBP-PX-15% with different thicknesses (20 and 50 μm) were compared with that of commercial AEM PiperION (40 μm) at different KOH concentrations (Fig. 6d–f). For 1 M KOH concentration (Fig. 6d),

the AEMWE based on the thinner QPBP-PX-15% membrane (20 μm) showed improved electrolysis performance compared to that of the thicker one (50 μm), due to reduced ohmic resistance. However, it was still slightly inferior to that of PiperION-based AEMWE, which could be due to the higher conductivity of PiperION. However, with higher KOH concentrations (6 M and 10 M), QPBP-PX-15%-based AEMWEs outperformed the PiperION-based ones (Fig. 6e and f). The ion conduction in the microporous channels of QPBP-PX-15% could potentially be enhanced at high alkali concentrations, thereby reducing mass transfer resistance and resulting in higher current densities at lower voltages. Particularly, the AEMWE based on QPBP-PX-15% (20 μm) showed a current density of 3000 mA cm^{-2} at 2.03 V with a KOH concentration of 6 M, which outperformed many AEMWEs that used PGM catalysts (Table 2).[45]

The short-term durability of AEMWE was assessed at 80 °C, 500 mA cm^{-2}, and in 6 M KOH solution. As shown in Fig. 7, the cell voltage remained stable after 80 hours of testing for durability. Furthermore, the detached aged AEM remained intact and transparent, except for some indentations caused by the catalytic electrode (Fig. 7). These results further demonstrated the good durability of the crosslinked AEMs.

3. Conclusions

An intrinsically microporous polyxanthene crosslinker, PX-SBI-5CBr, was synthesized successfully. It was reacted with PBP to prepare chemically crosslinked AEMs. Due to high rigidity of the ladder-like polyxanthene skeleton, the resultant crosslinked AEMs, QPBP-PX-*x*, had ultramicroporous structures and microphase-separated morphologies. This promoted the formation of ion transport channels, which was proven from their SAXS, AFM, and TEM analyses. Particularly, QPBP-PX-15% membrane showed high OH$^-$ and Cl$^-$ conductivities of 163.0 and 120.0 mS cm^{-1} at 80 °C, respectively. Meanwhile, QPBP-PX-15% showed moderate water uptake (WU = 40.3% at 80 °C), excellent dimensional stability (SR < 10% at 80 °C), and remarkable alkaline resistance (∼10% performance decline after treatment in 6 M NaOH solution at 80 °C for 40 days), possibly due to its highly rigid and crosslinked architecture. Furthermore, the QPBP-PX-15%-based AEMWE
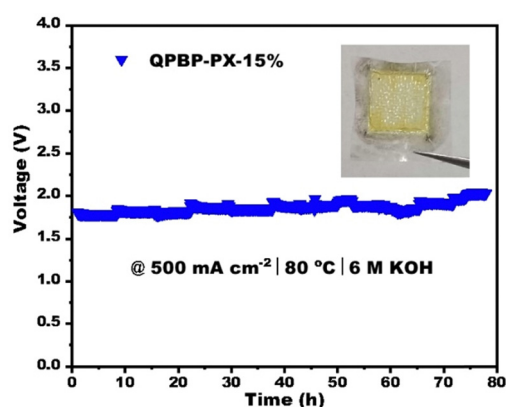

Fig. 7 Durability of QPBP-PX-15% based AEMWE at 80 °C, 500 mA cm^{-2}, and in 6 M KOH solution.

outperformed those based on commercial PiperION in high KOH concentrations. Specifically, the AEMWE based on QPBP-PX-15% and equipped with PGM-free catalysts acquired a current density of 3000 mA cm^{-2} at 2.03 V (compared to PiperION's 2.26 V) in 6 M KOH solution at 80 °C. The crosslinked microporous AEMs developed in this work showed great potential for applications in high-performance and cost-effective AEMWEs. This work also provides useful insights into the development of crosslinked AEMs for AEMWEs fed with high-concentration electrolytes.

Data availability

The data supporting this article have been included as part of the ESI.†

Conflicts of interest

There are no conflicts to declare.

Acknowledgements

References

1 N. Du, C. Roy, R. Peach, M. Turnbull, S. Thiele and C. Bock, *Chem. Rev.*, 2022, **122**, 11830.

2 Y. Yang, P. Li, X. Zheng, W. Sun, S. X. Dou, T. Ma and H. Pan, *Chem. Soc. Rev.*, 2022, **51**, 9620.

3 Q. Xu, L. Zhang, J. Zhang, J. Wang, Y. Hu, H. Jiang and C. Li, *Energy Chem.*, 2022, **4**, 100087.

4 U. Babic, M. Suermann, F. N. Büchi, L. Gubler and T. J. Schmidt, *J. Electrochem. Soc.*, 2017, **164**, F387.

5 D. Li, E. J. Park, W. Zhu, Q. Shi, Y. Zhou, H. Tian, Y. Lin, A. Serov, B. Zulevi, E. D. Baca, C. Fujimoto, H. T. Chung and Y. S. Kim, *Nat. Energy*, 2020, **5**, 378.

6 S. Stiber, N. Sata, T. Morawietz, S. A. Ansar, T. Jahnke, J. K. Lee, A. Bazylak, A. Fallisch, A. S. Gago and K. A. Friedrich, *Energy Environ. Sci.*, 2022, **15**, 109.

7 J. K. Lee, G. Anderson, A. W. Tricker, F. Babbe, A. Madan, D. A. Cullen, J. D. Arregui-Mena, N. Danilovic, R. Mukundan, A. Z. Weber and X. Peng, *Nat. Commun.*, 2023, **14**, 4592.

8 I. Vincent and D. Bessarabov, *Renewable Sustainable Energy Rev.*, 2018, **81**, 1690.

9 P. Chen and X. Hu, *Adv. Energy Mater.*, 2020, **10**, 2002285.

10 C. Niether, S. Faure, A. Bordet, J. Deseure, M. Chatenet, J. Carrey, B. Chaudret and A. Rouet, *Nat. Energy*, 2018, **3**, 476.

11 H. Jin, B. Ruqia, Y. Park, H. J. Kim, H. S. Oh, S. I. Choi and K. Lee, *Adv. Energy Mater.*, 2021, **11**, 2003188.

12 N. Chen and Y. M. Lee, *Prog. Polym. Sci.*, 2021, **113**, 101345.

13 M. G. Marino, J. P. Melchior, A. Wohlfarth and K. D. Kreuer, *J. Membr. Sci.*, 2014, **464**, 61.

14 J. Pan, C. Chen, L. Zhuang and J. Lu, *Acc. Chem. Res.*, 2012, **45**, 473.

15 H. Chen, K. T. Bang, Y. Tian, C. Hu, R. Tao, Y. Yuan, R. Wang, D. M. Shin, M. Shao, Y. M. Lee and Y. Kim, *Angew. Chem., Int. Ed.*, 2023, **62**, e202307690.

16 Y. Ma, C. Hu, G. Yi, Z. Jiang, X. Su, Q. Liu, J. Y. Lee, S. Y. Lee, Y. M. Lee and Q. Zhang, *Angew. Chem., Int. Ed.*, 2023, **62**, e202311509.

17 X. Wu, N. Chen, C. Hu, H. A. Klok, Y. M. Lee and X. Hu, *Adv. Mater.*, 2023, **35**, 2210432.

18 Y. Xie, S. Li, J. Pang and Z. Jiang, *J. Membr. Sci.*, 2023, **669**, 121333.

19 G. Xu, J. Pan, X. Zou, Z. Jin, J. Zhang, P. Fang, Q. Zhang, Z. Sun and F. Yan, *Adv. Funct. Mater.*, 2023, **33**, 2302364.

20 W. Song, K. Peng, W. Xu, X. Liu, H. Zhang, X. Liang, B. Ye, H. Zhang, Z. Yang, L. Wu, X. Ge and T. Xu, *Nat. Commun.*, 2023, **14**, 2732.

21 R. Weber, M. Klingenhof, S. Koch, L. Metzler, T. Merzdorf, J. Meier-Haack, P. Strasser, S. Vierrath and M. Sommer, *J. Mater. Chem. A*, 2024, **12**, 7826.

22 Z. Yang, R. Guo, R. Malpass-Evans, M. Carta, N. B. McKeown, M. D. Guiver, L. Wu and T. Xu, *Angew. Chem., Int. Ed.*, 2016, **55**, 11499.

23 Q. Wang, L. Huang, Z. Wang, J. Zheng, Q. Zhang, G. Qin, S. Li and S. Zhang, *Macromolecules*, 2022, **55**, 10713.

24 C. Hu, H. W. Kang, S. W. Jung, M. L. Liu, Y. J. Lee, J. H. Park, N. Y. Kang, M. G. Kim, S. J. Yoo, C. H. Park and Y. M. Lee, *Adv. Sci.*, 2023, **11**, 2306988.

25 S. Q. Fu, B. Hu, J. H. Ge, M. Z. Zhu, P. P. Huang, B. Xue, N. Li and P. N. Liu, *Macromolecules*, 2023, **56**, 6037.

26 C. Hu, N. Y. Kang, H. W. Kang, J. Y. Lee, X. Zhang, Y. J. Lee, S. W. Jung, J. H. Park, M. G. Kim, S. J. Yoo, S. Y. Lee, C. H. Park and Y. M. Lee, *Angew. Chem., Int. Ed.*, 2024, **63**, e202316697.

27 Y. Lee, K. Min, J. Choi, G. Choi, H. Kim and T. H. Kim, *J. Mater. Chem. A*, 2023, **11**, 25008.

28 P. Zuo, Y. Li, A. Wang, R. Tan, Y. Liu, X. Liang, F. Sheng, G. Tang, L. Ge, L. Wu, Q. Song, N. B. McKeown, Z. Yang and T. Xu, *Angew. Chem., Int. Ed.*, 2020, **59**, 9564.

29 D. Pan, S. Chen and P. Jannasch, *ACS Macro Lett.*, 2023, **12**, 20.

30 B. Xue, Z. Zheng, H. Qian, Z. Wang and J. Yan, *Macromolecules*, 2024, **57**, 3376.

31 J. S. Olsson, T. H. Pham and P. Jannasch, *Adv. Funct. Mater.*, 2018, **28**, 1702758.

32 B. Liu, T. Li, Q. Li, S. Zhu, Y. Duan, J. Li, H. Zhang and C. Zhao, *J. Membr. Sci.*, 2022, **660**, 120816.

33 H. Zhu, Y. Li, N. Chen, C. Lu, C. Long, Z. Li and Q. Liu, *J. Membr. Sci.*, 2019, **590**, 117307.

34 X. Wang, Z. Fang, M. Zhang, S. Xie, D. Xie, P. Liu, S. Wang, F. Cheng and T. Xu, *J. Membr. Sci.*, 2024, **700**, 122717.

35 X. Wu, N. Chen, H. A. Klok, Y. M. Lee and X. Hu, *Angew. Chem.*, 2022, **134**, e202114892.

36 S. Kim, S. H. Yang, S. H. Shin, H. J. Cho, J. K. Jang, T. H. Kim, S. G. Oh, T. H. Kim, H. Han and J. Y. Lee, *Energy Environ. Sci.*, 2024, **17**, 5399.

37 M. G. Marino, J. P. Melchior, A. Wohlfarth and K. D. Kreuer, Hydroxide, halide and water transport in a model anion exchange membrane, *J. Membr. Sci.*, 2014, **464**, 61.

38 L. Han, S. Gong, X. Zhang, M. Yang, X. Yan, G. He and F. Zhang, *J. Mater. Chem. A*, 2024, **12**, 6341.

39 N. Chen, H. H. Wang, S. P. Kim, H. M. Kim, W. H. Lee, C. Hu, J. Y. Bae, E. S. Sim, Y. Chung, J. Jang, S. J. Yoo, Y. Zhuang and Y. M. Lee, *Nat. Commun.*, 2021, **12**, 2361.

40 X. Su, S. Nan, W. Wei, S. Xu and R. He, *J. Membr. Sci.*, 2023, **683**, 121843.

41 L. Qi, X. Wang, G. Chao, N. Li and X. Zhang, *J. Membr. Sci.*, 2023, **687**, 122057.

42 K. M. Meeka, C. M. Antunesa, D. J. Strassera, Z. R. Owczarczyka, A. C. Yang-Neyerlina and B. S. Pivovara, *ECS Trans.*, 2019, **92**, 723.

43 M. Zeng, X. He, J. Wen, G. Zhang, H. Zhang, H. Feng, Y. Qian and M. Li, *Adv. Mater.*, 2023, **35**, 2306675.

44 T. Kou, S. Wang, R. Shi, T. Zhang, S. Chiovoloni, J. Q. Lu, W. Chen, M. A. Worsley, B. C. Wood, S. E. Baker, E. B. Duoss, R. Wu, C. Zhu and Y. Li, *Adv. Energy Mater.*, 2020, **10**, 2002955.

45 T. Caielli, A. R. Ferrari, S. Bonizzoni, E. Sediva, A. Caprì, M. Santoro, I. Gatto, V. Baglio and P. Mustarelli, *J. Power Sources*, 2023, **557**, 232532.

46 N. Chen, S. Y. Paek, J. Y. Lee, J. H. Park, S. Y. Lee and Y. M. Lee, *Energy Environ. Sci.*, 2021, **14**, 6338.

47 R. A. Krivina, G. A. Lindquist, S. R. Beaudoin, T. N. Stovall, W. L. Thompson, L. P. Twight, D. Marsh, J. Grzyb, K. Fabrizio, J. E. Hutchison and S. W. Boettcher, *Adv. Mater.*, 2022, **34**, 2203033.

48 O. Boström, S. Y. Choi, L. Xia, S. Meital, F. Lohmann-Richters and P. Jannasch, *J. Mater. Chem. A*, 2023 **11**, 21170.